minerals

MDPI

Article

A DFT Study of the Mechanical Properties of a Lizardite Slab Reinforced by Graphene and Hexagonal Boron Nitride

Anne Karollynne Castro Monteiro [1], Consuelo Alves da Frota [2], Cicero Mota [3], Angsula Ghosh [4] and Hidembergue Ordozgoith da Frota [4,*]

[1] Graduate Program in Materials Science and Engineering (PPGCEM), Federal University of Amazonas, Manaus 69080-900, Brazil; annekarollynne@gmail.com
[2] Department of Civil Engineering, Federal University of Amazonas, Manaus 69080-900, Brazil; cafrota@ufam.edu.br
[3] Department of Mathematics, Federal University of Amazonas, Manaus 69080-900, Brazil; mota@ufam.edu.br
[4] Department of Materials Physics, Federal University of Amazonas, Manaus 69080-900, Brazil; angsula@ufam.edu.br
* Correspondence: hfrota@ufam.edu.br

Abstract: The stacking of two-dimensional atomic-level thickness materials onto hexagonal boron nitride (h-BN) and graphene (Gr) not only significantly enhances their properties, but also exhibits a multitude of exceptional characteristics, promising widespread applications across various fields. Clay minerals hold profound significance in scientific research not only because of their abundance but also because of their application in geology, environmental science, materials science, and biotechnology. We present a study that uses density functional theory (DFT) to analyze the effect on the mechanical properties of lizardite slab-reinforced Gr or h-BN monolayers. In addition to the reference lizardite slab (Liza-2D), six composites were studied: a monolayer of Gr (h-BN) over the octahedral face of a pristine lizardite slab (Liza-Gr1 (Liza-BN1)), a monolayer of Gr (h-BN) under the tetrahedral face of a pristine lizardite slab (Liza-Gr2(Liza-BN2)), and a pristine lizardite slab sandwiched between two Gr (h-BN) monolayers (Liza-Gr3(Liza-BN3)). We observed that reinforcement by Gr or h-BN significantly increased the bulk, Young's and shear moduli of the composites. Taking into account that the Gr and h-BN sheets interact weakly by van der Waals interactions with the lizardite slab surface, we estimated the Young's and shear moduli of the composites by the *Rule of Mixtures* and obtained a reasonable agreement with those from DFT calculations.

Keywords: lizardite; DFT; mechanical properties; bilayers heterostructures

Academic Editor: Andrey G. Kalinichev

Received: 16 December 2024
Revised: 31 December 2024
Accepted: 4 January 2025
Published: 7 January 2025

Citation: Monteiro, A.K.C.; Frota, C.A.d.; Mota, C.; Ghosh, A.; Frota, H.O.d. A DFT Study of the Mechanical Properties of a Lizardite Slab Reinforced by Graphene and Hexagonal Boron Nitride. *Minerals* **2025**, *15*, 53. https://doi.org/10.3390/min15010053

1. Introduction

Since the pioneering work of Novoselov et al. [1,2], graphene has fascinated researchers worldwide owing to its electronic, transport, optical and mechanical properties [3], stimulating interest in two-dimensional materials [4,5] with potential technological applications. This exploration spans metallic [6], semiconductor [7–9] and superconductor materials [10]. In the last few years, there has been a notable surge in both experimental and theoretical investigations into the mechanical characteristics of layered materials, as evidenced by the significant number of review articles on this subject [11–17].

Although the experimental measurement of the elastic modulus of two-dimensional materials remains a great challenge, considerable progress has been made in this effort using atomic force microscopy (AFM) technology, particularly in indenting suspended

two-dimensional samples over patterned holes. The elastic modulus was obtained from nanoindentation, which produces a spatial resolution on the nanometer scale to map the mechanical properties along the membrane. Moreover, theoretical methods, such as the mechanical model for single and doubly clamped beams under tension, the finite element method and density functional theory have been used in conjunction for the above purposes [18–21].

Even though the AFM technique has not yet been used to measure the mechanical properties of the clay mineral lizardite reinforced with graphene and boron nitride, which is the focus of this study, we will present some applications of this technique to these properties in nanometric scale materials. Using AFM together with theoretical mechanical models, Frank et al. [18] determined the Young's modulus of suspended stacks of graphene layers over photolithographically defined trenches in silicon dioxide films on a silicon substrate. For suspended graphene sheets thinner than 10 nm, they obtained a Young's modulus of 0.5 TPa. Poot et al. [19] measured the mechanical properties of few-layer graphene and graphite flakes suspended over circular holes using the atomic force microscope. They obtained the bending rigidity and tension in the membrane by fitting a mechanical continuum model to the spatial profile of the spring constant data and concluded that this technique is not limited to multilayer graphene flakes but can be applied to membranes of any kind.

In a pioneering work, Lee et al. [20] used AFM technology to measure for the first time the force-displacement behavior of a suspended monolayer of graphene over open holes, which was interpreted based on the nonlinear elastic stress-strain response. They obtained an incredible value of 1.0 TPa for the Young's modulus of graphene, the highest value for a known material. Moreover, it is twice the result obtained in reference [18] for stacks of graphene layers, and has an intrinsic strength of 130 GPa. Falin et al. [21] employed exfoliation to fabricate suspended boron nitride nanosheets. Employing the same indentation and fitting methodologies utilized for graphene, they experimentally determined, for the first time, the Young's modulus and strength of a monolayer of h-BN, an insulator with an indirect band gap close to 6.0 eV, yielding values of 0.865 GPa and 70.5 GPa, respectively. Although the electronic properties and chemical and thermal stabilities of graphene and hexagonal boron nitrite are very different, their mechanical properties are similar, with h-BN being as strong as graphene. The authors [21] suggested that h-BN nanosheets are one of the strongest insulating materials and, like graphene, are ideal for applications such as the mechanical reinforcement of ceramic and metal matrix composites.

Motivated by the success of the experimental determination of the elastic properties of a graphene monolayer, Bertolazzi et al. [22] extended the AFM and nanoindentation methods to other layered materials, including single and bilayers of molybdenum disulfide (MoS_2). These materials were obtained using a micromechanical cleavage technique, similar to the method used to produce graphene from bulk crystals. For suspended mono and bilayer MoS_2 they obtained Young's moduli of 270 GPa and 200 GPa, respectively. Yang et al. [23] used a scanning electron microscope chamber and determined the average Young's modulus to be 177.2 GPa for the uniform in-plane loading of a freestanding membrane of 2D molybdenum diselenide ($MoSe_2$). Liu et al. experimentally determined the Young's modulus of a suspended monolayer of MoS_2 using the chemical vapor deposition method [24]. The value of 268 GPa is consistent with that of an exfoliated monolayer [23].

Considering that the suspension method relies on the precise alignment of the AFM probe with the center of the suspended membrane, which is a difficult challenge, and that fabricating the pre-patterned substrate and transferring the sample onto the designated holes is nontrivial, Li et al. [25] proposed a new method to directly map the in-plane Young's modulus of 2D materials on the substrate with high spatial resolution. They used

bimodal atomic force microscopy to measure the in-plane Young's modulus of monolayer and bilayer MoS_2 on Si/SiO_2 substrate. The above technique was combined with the finite element method to decouple the Young's modulus of monolayer MoS_2 based on the effect of substrate stiffness on deformation. They obtained 265 ± 13 GPa for the Young's modulus of the monolayer MoS_2, which is in good agreement with the results previously obtained by the suspension technique and is indistinguishable from the result for bilayer MoS_2 [25].

From a structural point of view, considering the high strength of Gr and h-BN, it is expected that the deposition of a Gr or a h-BN sheet on a substrate enhances its strength. Several studies have taken this possibility into account [26–33]. In the last few years, graphene has been used to reinforce metal matrix composites, such as Al, Zn, Mg, Cu, Ni and Ti [29–31,34]. It has also been utilized to reinforce polymer [35,36] and ceramics [37,38] matrices. Similar to graphene, h-BN monolayers have also been used as reinforcement to enhance the mechanical performance of materials [39–43]. It has been observed that the measured tensile strength values depend on different factors, such as the production method of the composites, different types of reinforcement materials such as graphene (h-BN), graphene (h-BN) nanoplalets or graphene (hBN) nanosheets, and the surface treatment of the matrix material [34]. For example, depending on the sample preparation, the tensile strength of the Al composites reinforced with 0.3 wt.% graphene nanosheets, fabricated using powder metallurgy, can be 62% higher [44] or 11% higher [45] than that of the pure Al matrix.

Lizardite, a hydrated magnesium silicate $[Mg_3(Si_2O_5)(OH)_4]$, is a greenish mineral rock from the kaolinite-serpentine group [46], the most abundant serpentine, with a 1:1 type mineral structure. It is a layered material composed of stacked two basic units: an octahedral layer $[Mg\ O_{6-n}(OH)_n]$ and a tetrahedral layer $[SiO_2^{4-}]$, which are joined by common oxygen atoms [47], as shown in Figure 1a. In addition to its potential environmental friendliness [48,49], with its high capacity for carbon dioxide sequestration [50], lizardite has attracted considerable attention because of its diverse technological applications [51].

The aim of this study is to investigate the mechanical properties of the clay mineral lizardite reinforced by graphene (Gr) and hexagonal boron nitrite (h-BN), using ab initio calculations within the framework of density functional theory (DFT). The interest in studying composites of lizardite reinforced with graphene or boron nitride can lead to the development of new materials with superior mechanical properties, potentially surpassing those of traditional materials used in various industries, such as the construction industry. Understanding the mechanical behavior of these composites can optimize their performance in real-world applications, ensuring they meet specific strength, durability, and flexibility requirements.

To achieve the objectives of this study we will obtain the mechanical properties of lizardite reinforced with Gr and h-BN considering seven superstructures: (i) a slab of pristine lizardite extracted from the crystal, formed by octahedral and tetrahedral layers (Liza) (Figure 1a); (ii) a monolayer of Gr (h-BN) over the octahedral face of the pristine lizardite slab (Liza-Gr1) (Liza-BN1) (Figure 1b,e); (iii) a monolayer of Gr (h-BN) under the tetrahedral face of the pristine lizardite slab (Liza-Gr2) (Liza-BN2) (Figure 1c,f); (iv) and a pristine lizardite slab sandwiched between two Gr (h-BN) monolayers (Liza-Gr3) (Liza-BN3) (Figure 1d,g). The computational method used in this study is presented in the second section, followed by the results and discussion in the third section. Finally, in the last section, we present our conclusions.

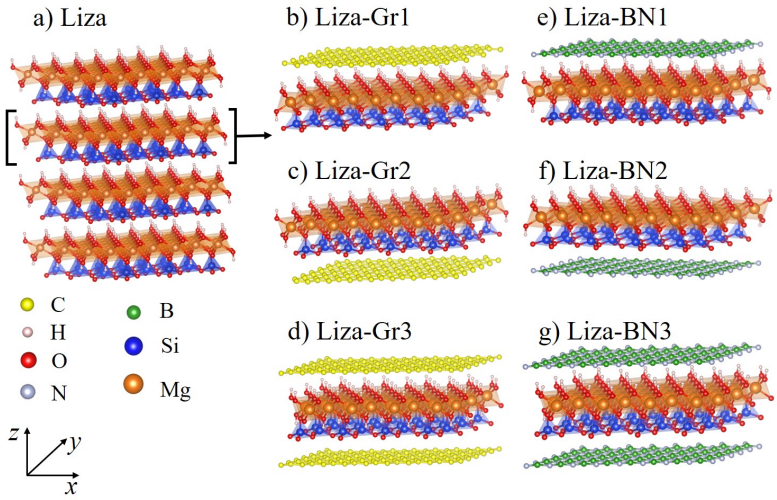

Figure 1. The superstructures to study the contribution of graphene and h-BN for the reinforcement of lizardite: (**a**) Liza—a slab extracted from the pristine lizardite layered crystal; (**b**,**e**) Liza-Gr1 (Liza-BN1)—a monolayer of Gr (h-BN) over the octahedral face of the pristine lizardite slab; (**c**,**f**) Liza-Gr2 (Liza-BN2)—a monolayer of Gr (h-BN) under the tetrahedral face of the pristine lizardite slab; (**d**,**g**) Liza-Gr3 (Liza-BN3)—a slab of pristine lizardite sandwiched between two monolayers of Gr (h-BN).

2. Methodology

2.1. The Ab Initio Calculations

The ab initio calculations were carried out using density functional theory (DFT) as is performed in the Quantum Espresso (QE) package [52], using the ultrasoft pseudopotential type. The exchange-correlation functional was implemented in the generalized gradient approximation (GGA) as proposed by Perdew, Burke and Ernzerhof (PBE) [53], taking into account the van der Waals interaction using the Grimme-D2 methods [54,55]. Geometry optimization was performed using the BFGS quasi-Newton algorithm, with convergence thresholds of forces and total energy for ionic minimization established at 10^{-6} eV/Å and 10^{-5} eV, respectively. The kinetic energy cutoffs for the summation related to the calculation of the wave functions and the charge density were 0.8 keV and 8.2 keV, respectively. For Brillouin zone sampling a Monkhorst–Pack grid [56,57] was constructed in the k space of dimensions $6 \times 6 \times 1$. A vacuum slab of at least 18 Å in the z-direction perpendicular to the lizardite slab plane was set to avoid interactions between adjacent cells. Graphic representations of the superstructures were created using the VESTA package [58].

2.2. Mechanical Properties

The elastic constants were determined from the second-order elastic stiffness matrix $C_{ij} = \partial^2 E / \partial \varepsilon_i \partial \varepsilon_j) / V_0$ (in Voigt notation [59]), where E is the crystal energy, ε is the strain and V_0 is the equilibrium volume, according to the Thermo_pw package [60], an integral component of the Quantum Espresso software. The mechanical stability was verified by the criterion that all eigenvalues of the elastic stiffness matrix were greater than zero [61–64]. Owing to the presence of vacuum between the layers, the calculation of the stiffness constants C_{ij} was carried out in a three-dimensional space. As is customary, to convert the C_{ij} tensor obtained for a bulk unit cell with height h (the sum of the vacuum and slab thickness) to a 2D C_{ij}^{2D} tensor, we employed the relation $C_{ij}^{2D} = h \times C_{ij}$ [20,65]. Assuming that the relaxation process occurs under hydrostatic pressure [66] in two dimensions,

the layer modulus K^{2D}, 2D Young's modulus Y^{2D}, 2D shear modulus G^{2D} and 2D Poisson's ratio ν^{2D} are defined as follows [67,68]:

$$K^{2D} = \frac{1}{4}\left[C_{11}^{2D} + C_{22}^{2D} + 2C_{12}^{2D}\right] \quad (1)$$

$$Y^{2D} = \frac{C_{11}^{2D}C_{22}^{2D} - (C_{12}^{2D})^2}{C_{11}^{2D}} \quad (2)$$

$$G^{2D} = C_{66}^{2D} \quad (3)$$

$$\nu^{2D} = \frac{K^{2D} - G^{2D}}{K^{2D} + G^{2D}} \quad (4)$$

The longitudinal (v_L) and transverse (v_T) sound velocities were obtained from the Christoffel equation [69] for hexagonal lattice and are given by

$$v_L = \sqrt{\frac{K^{2D} + G^{2D}}{\rho^{2D}}} \quad (5)$$

$$v_T = \sqrt{\frac{G^{2D}}{\rho^{2D}}}, \quad (6)$$

where ρ^{2D} is the two-dimension mass density.

Given that the slab possesses a finite thickness t along the out-of-plane direction (z), to scale the mechanical properties for quasi-2D systems, denoted by the superscript $3D$, we divided the aforementioned 2D elastic moduli by the slab thickness t: $K^{3D} = K^{2D}/t$, $Y^{3D} = Y^{2D}/t$ and $G^{3D} = G^{2D}/t$ [67,70].

2.3. Supercell

To construct the superstructures Liza-Gr1 (Liza-BN1), Liza-Gr2 (Liza-BN2) and Liza-Gr3 (Liza-BN3) we considered a supercell of Gr (h-BN) containing 2×2 unit cells, with lattice parameter $a_{Gr(BN)} = 4.92(4.87)$ Å, and 1×1 unit cell of lizardite with lattice parameter $a_{Liza} = 5.29$ Å. The lateral mismatch between the lizardite slab and graphene (BN) sheet was $100 \times (a_{Liza} - a_{Gr(BN)})/a_{Liza} = 7.0\%(7.9\%)$. After the geometric optimization process of the above superstructures, the Gr (BN) sheet underwent lateral stretching while the lizardite slab shrank laterally. For the Liza-Gr1 (Liza-BN1) and Liza-Gr2 (liza-BN2) superstructures, the lizardite slab shrank by 4.5% (4.5%) and the Gr (BN) sheet stretched by 2.7% (3.7%), whereas for the Liza-Gr3 (Liza-BN3) superstructure, the lizardite slab shrank by 5.8% (5.8%) and the graphene sheet stretched by 1.2% (2.3%). We could increase the size of the supercells to reduce mismatches; however, this would lead to a significant increase in the computational cost.

3. Results and Discussion

The two- and quasi-two-dimensional elastic constants, C_{ij}^{2D} and C_{ij}^{3D}, respectively, are presented in Table 1. The mechanical properties derived from the elastic constants (C_{ij}^{2D} and C_{ij}^{3D}), are shown in Table 2: the 2D layer modulus K^{2D}, Young's modulus Y^{2D} and shear modulus G^{2D}, as well as the quasi-two-dimensional bulk modulus K^{3D}, Young's modulus Y^{3D} and shear modulus G^{3D}, 2D Poisson's ratio ν^{2D} and longitudinal, transversal and average velocities v_L, v_T and v_a, respectively. In order to validate the methodology used in this work, we compared our results for Gr (h-BN) with those in the literature, assuming, as is habitual, an effective thickness $t = 3.35$ Å ($t = 3.33$ Å) for the Gr [20,65] (h-BN [71]) monolayer. These values were obtained from the distance between the two crystal planes of graphite (hexagonal boron nitride). To the best of our knowledge, there are

no theoretical or experimental results in the literature regarding the mechanical properties of lizardite/Gr(BN) layered superstructures. Nevertheless, there are theoretical results for the elastic moduli of bulk lizardite [72,73]. Although there are no complete experimental results on the elastic moduli of lizardite, there are measurements of compressibility of clay minerals [74,75], from which the bulk modulus is obtained. As this clay mineral exhibits a layered structure with weak van der Waals interactions between its layers, it is also pertinent to highlight the differences that arise by comparing the bulk mechanical properties of quasi-two-dimensional (3D) lizardite slab with those of the bulk lizardite crystals.

Table 1. The 2D elastic constants C_{ij}^{2D} and quasi-two-dimensional elastic constants C_{ij}^{3D}, the unit cell height h and the slab thickness t. We used the thickness $t = 3.35$ Å [67,70] and $t = 3.33$ Å [71] for Gr and h-BN, respectively, to obtain the quasi-two-dimensional C_{ij}^{3D}.

Compound	h (Å)	t (Å)	C_{11}^{2D} (N/m)	C_{12}^{2D} (N/m)	C_{22}^{2D} (N/m)	C_{66}^{2D} (N/m)	C_{11}^{3D} (GPa)	C_{12}^{3D} (GPa)	C_{22}^{3D} (GPa)	C_{66}^{3D} (GPa)
Liza-2D	29.0	5.29	157.95	57.47	158.06	52.95	298.82	108.73	299.03	100.17
Liza-Gr1	29.0	7.66	459.75	101.45	459.62	181.21	600.05	132.41	599.88	236.51
Liza-Gr2	29.0	8.42	457.18	103.55	457.99	177.71	542.77	122.94	543.74	210.98
Liza-Gr3	30.0	10.67	824.85	141.45	824.76	346.70	773.26	132.60	773.17	325.01
Liza-BN1	29.0	7.61	432.94	113.76	430.32	167.11	568.90	149.49	565.45	219.59
Liza-BN2	29.0	8.42	439.87	105.01	439.70	173.15	522.195	124.67	521.99	205.55
Liza-BN3	30.0	10.62	767.84	200.25	771.00	284.15	722.76	188.50	725.74	267.46
Graphene [a]	20.0	3.35	353.00	63.77	353.00	144.61	1053.73	190.36	1053.73	431.69
Graphene [b]	15.0	3.35	352.70	60.90	352.70	145.90	1052.84	181.79	1052.84	435.52
h-BN [a]	20.0	3.33	325.20	84.58	325.20	120.31	976.59	254.00	976.59	361.29
h-BN [c]	–	3.33	291.00	62.00	291.00	114.50	873.87 [f]	186.19 [f]	873.87 [f]	343.84 [f]
Lizardite [d]	–	–	–	–	–	–	217.20	76.20	217.20	70.50
Lizardite [e]	–	–	–	–	–	–	215.72	74.22	215.72	70.50

[a] This work. [b] Refs. [67,70] (theory). [c] Ref. [76] (theory). [d] Ref. [72] (theory). [e] Ref. [73] (theory). [f] Obtained from Ref. [76] assuming $t = 3.33$ Å.

Table 2. The 2D layer modulus K^{2D}, Young's modulus Y^{2D} and shear modulus G^{2D}, the quasi-two-dimensional bulk modulus K^{3D}, Young's modulus Y^{3D} and shear modulus G^{3D}, the 2D Poisson's ratio ν^{2D} and the longitudinal v_L, transversal v_T and average velocities v_a.

Compound	K^{2D} (N/m)	K^{3D} (GPa)	Y^{2D} (N/m)	Y^{3D} (GPa)	G^{2D} (N/m)	G^{3D} (GPa)	ν^{2D} (no units)	v_L (km/s)	v_T (km/s)	v_a (km/s)
Liza-2D	107.74	203.83	137.05	259.38	52.95	100.17	0.36	9.20	5.28	7.50
Liza-Gr1	280.57	366.19	437.36	570.75	181.21	236.51	0.22	12.83	8.04	10.71
Liza-Gr2	280.57	333.10	433.76	515.44	177.71	210.98	0.23	12.79	7.96	10.65
Liza-Gr3	483.13	452.91	800.59	750.47	346.70	325.01	0.17	15.13	9.78	12.74
Liza-BN1	272.20	358.33	403.86	527.78	167.11	219.59	0.26	9.07	5.59	7.54
Liza-BN2	272.70	323.38	414.79	492.32	173.15	205.55	0.24	9.13	5.69	7.61
Liza-BN3	484.40	456.37	716.83	675.19	284.15	267.46	0.26	10.52	6.40	8.71
Graphene [a]	208.38	622.04	341.48	1019.34	144.61	431.69	0.18	21.53	13.78	18.08
Graphene [b]	206.80	617.31	342.20	1021.49	145.90	435.52	0.17	–	–	–
Graphene [e,f]	–	–	340.00 [d]	1014.93 [d]	–	–	–	19.90 [e]	12.90 [e]	–
h-BN [a]	204.89	615.30	303.21	910.53	120.31	361.29	0.26	20.13	12.25	16.66
h-BN [c]	–	–	–	716–977	–	–	–	–	–	–
h-BN [d]	–	–	–	865.00	–	–	–	–	–	–
Lizardite [g]	–	72.46	–	118.93	–	47.21	0.26	6.85	5.28	–
Lizardite [h]	–	68.00	–	–	–	–	0.26	6.50	3.5	–

[a] This work. [b] Ref. [67] (theory). [c] Ref. [77] (theory). [d] Ref. [21] (experiment). [e] Ref. [20] (experiment). [f] Ref. [78] (experiment). [g] Ref. [72] (theory). [h] Ref. [74] (experiment).

The elastic constants C_{ij}^{2D} and C_{ij}^{3D} of the superstructures Liza-2D, Liza-Gri, and Liza-BNi ($i = 1, 2$ and 3) and some results from the literature are presented in Table 1. The corresponding unit cell height h and the slab thickness t used to calculate C_{ij}^{2D} and C_{ij}^{3D} from the results obtained from the supercell with a vacuum slab are shown. The present calculations of the elastic constants of Gr and h-BN are in good agreement with the results of references [67,70], as well as with those of reference [76]. The reinforcement of an individual lizardite slab with Gr or h-BN sheets has an elastic constant C_{11}^{2D} that is slightly smaller than the sum of the elastic constants C_{11}^{2D} of the two components. For instance, regarding the superstructures Liza-Gr1 (Liza-BN1) and Liza-Gr2 (Liza-BN2), where an isolated lizardite slab (Liza-2D) is reinforced by a Gr (h-BN) sheet, the elastic constants C_{11}^{2D} are approximately equal to 95% of the sum of the corresponding elastic constants of the Liza-2D slab and Gr

(h-BN) sheet. Considering the Liza-Gr3 (Liza-BN3) superstructure, where the lizardite slab is doubly reinforced by two monolayers of Gr (h-BN), these values are approximately 90%. Comparing the lizardite slab with the bulk lizardite, we observe that the elastic constants C_{11}^{3D} of lizardite (Liza-2D) are approximately 40% larger than that of the bulk lizardite crystal [72,73]. It is more interesting to compare the quasi-two-dimensional elastic constant C_{11}^{3D} (in GPa) of the pristine lizardite slab with the corresponding elastic constants of the lizardite slab reinforced by Gr and h-BN. When the lizardite slab was reinforced by Gr or h-BN, a significant increase was observed in the quasi-two-dimensional elastic constants C_{11}^{3D}. For Liza-Gr1 (Liza-BN1), Liza-Gr2 (Liza-BN2) and Liza-Gr3 (Liza-BN3), C_{11}^{3D} increased by 100% (90%), 81% (75%) and 159% (142%), respectively. The configurations with Gr (h-BN) sheet placed on the octahedral surface present an increase in C_{11}^{3D} of approximately 10% greater than if the sheets were placed on the tetrahedral surface.

Table 2 lists the elastic moduli, Poisson's ratio, and longitudinal, transverse and average velocities. Our results (superscript *a*) for the Gr sheet are in good agreement with the theoretical predictions (superscript *b*) [67] and experimental measurements (superscripts *c* and *d*) [20,78]. Although graphene sheets have been extensively studied owing to their elastic properties, the same is not true for h-BN sheets. Our result of 910.53 for the Young's modulus of h-BN sheets falls within the range of 716 to 977 GPa reported in the literature obtained using various theoretical methods [77]. It is interesting to note the substantial enhancement in the quasi-two-dimensional bulk modulus K^{3D} of a lizardite slab (Liza-2D) in relation to the bulk modulus of the lizardite crystal. From our results, the K^{3D} of the superstructure Liza-2D (203.67 GPa) is approximately three times the experimental (68.0 GPa) [74] and theoretical (72.46 GPa) [72] values for the lizardite crystal. This correlation is logical considering that the bulk lizardite crystal exhibits a planar structure formed by stacking 1:1 layers composed of one octahedral and one tetrahedral sheet that interact with each other through weak van der Waals forces. N. Hilairet et al. [75] experimentally observed that the bulk compressibility of lizardite is dominated by that (inverse of bulk modulus) along the *c* axis, which can be attributed to the weaker bonds between the slabs, in contrast to the strong ionic bonds in the in-plane directions. They observed that the crystal along the *c* axis is three times more compressible than those along the *a* and *b* axes. From DFT calculations of the mechanical properties of bulk lizardite crystals, Gusmão et al. [72] found the ratio of $c_{11}/c_{33} = 2.50$, implying that under uniaxial stress, the in-plane stiffness is much larger than the out-of-plane *c*-axis. Therefore, both the experimental and theoretical results on the compressibility of bulk lizardite crystals corroborate our calculation, confirming the tripling of the quasi-two-dimensional bulk modulus of a lizardite slab compared to that of the bulk lizardite crystal.

The reinforcement of the lizardite slab by the Gr and h-BN layers significantly enhances its elastic moduli, as illustrated in Figure 2a,b, respectively, and listed in Table 2. The data for Liza-2D are represented by blue, Liza-Gr1 and Liza-BN1 by brown color, Liza-Gr2 and Liza-BN2 by gray and Liza-Gr3 and Liza-BN3 by yellow. It is interesting to highlight that for the superstructures Liza-Gr1 and Liza-Gr2, as well as Liza-BN1 and Liza-BN2, in which the lizardite slab is singly reinforced by Gr and h-BN sheets, respectively, the two-dimensional layer modulus K^{2D}, Young's modulus Y^{2D} and shear modulus G^{2D} increase by approximately three times the corresponding value of Liza-2D. For the superstructure Liza-Gr3 and Liza-BN3, which is doubly reinforced by Gr and h-BN sheets, respectively, the enhancement in K^{2D} is approximately four times that in Y^{2D} and G^{2D} is approximately six times that of Liza-2D. Analyzing the quasi-two-dimensional elastic moduli, for Liza-Gr1, Liza-Gr2, Liza-Gr3, and their counterparts Liza-BN1, Liza-BN2 and Liza-BN3, the quasi-two-dimensional bulk modulus K^{3D} increases by approximately two times and Y^{3D} and G^{3D} enhance by approximately three times the respective values for Liza-2D. The effects of

reinforcing lizardite with graphene and h-BN sheets are practically compatible, that is, both significantly enhance the mechanical properties of the lizardite slab, resulting in stronger composite materials. These enhancements are observed experimentally in the mechanical properties of other composites reinforced with graphene, such as the increase of 62% [44] and 93% [79] of the tensile strength of the Al composite reinforced with only 0.3 wt.% and 0.54 wt.% of graphene nanosheets, respectively.

Regarding sound conduction in these new materials, we observed from Table 2 that the large increase in the elastic moduli of lizardite reinforced by GR or h-BN considerably enhanced the sound speed in these superstructures owing to the contributions of the sound propagation channels in the Gr and h-BN sheets.

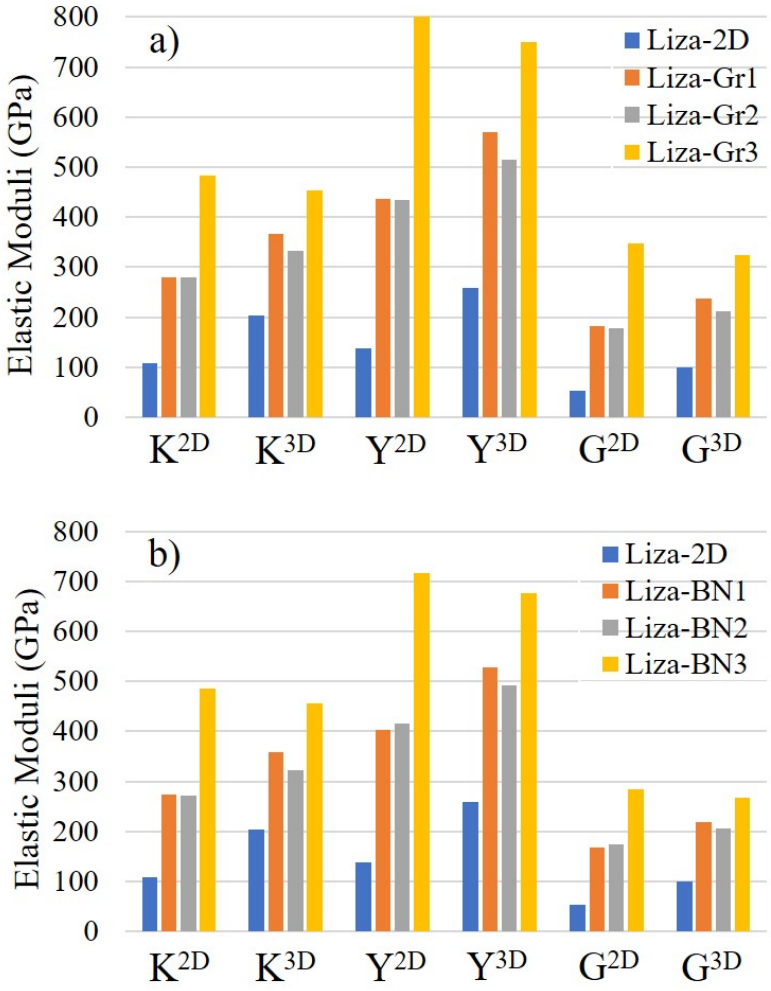

Figure 2. Comparison of the bulk, Young's and shear moduli of the composites with the reference Liza-Gr: (**a**) Liza-Gr1, Liza-Gr2 and Liza-Gr3; (**b**) Liza-BN1, Liza-BN2 and Liza-BN3. The reinforcement by both Gr and h-BN sheets significantly increases the mechanical properties of lizardite slab.

Previous works have obtained an interlayer binding energy of 25.0 meV and 28.0 meV for Liza-Gr1 and Liza-Gr2 [80], as well as 39.0 meV and 26.0 meV for Liza-BN1 and Liza-BN2 [81], respectively. These values are lower than the experimental values of 70.0 meV [82] and 104.0 meV [83] obtained for the graphite interlayers with different methods. From these considerations, we assume that there is a weak interaction between Gr or h-BN sheets and the lizardite slab. Thus, it is reasonable to use the well-known Rule of Mixtures (ROM) [84] to estimate the effective Young's modulus of the Gr(BN)/lizardite slab composites. To represent this actual system, we just used the slab model defined by Equations (7)–(9), which were obtained using the assumption that the lizardite, graphene and boron nitride slabs

are parallel, with the same length and undergo the same amount of deformation, which is a reasonable conjecture, because they are contained in the same crystal supercell. The thicknesses of the Gr (h-BN) sheet and lizardite slab, as well as their respective Young's moduli, were essential for the calculations. Considering that the components of the composites have the same length and width and different thicknesses t, the effective Young's (Y_{eff}) and shear (G_{eff}) moduli are given by

$$Y_{\text{eff}} = fY_{\text{Gr}} + (1-f)Y_{\text{Liza-2D}} \quad (7)$$

$$G_{\text{eff}} = fG_{\text{Gr}} + (1-f)G_{\text{Liza-2D}}, \quad (8)$$

where f is the ratio of the Gr (h-BN) sheet thickness ($t_{Gr(h-BN)}$) to the total sample thickness ($t_{Gr,h-BN} + t_{Liza-2D}$),

$$f = \frac{t_{Gr(h-BN)}}{t_{Gr(h-BN)} + t_{Liza-2D}}, \quad (9)$$

$t_{Liza-2D}$ is the lizardite slab thickness, $Y_{\text{Gr(h-BN)}}$ ($Y_{\text{Liza-2D}}$) and $G_{\text{Gr(h-BN)}}$ ($G_{\text{Liza-2D}}$) are the Young's and shear moduli of the Gr (h-BN) sheet (lizardite slab), respectively. Using the Equations (7) and (8) with the data in Table 2, we obtained the Gr(h-BN)/Liza-2D slab composite $Y_{\text{eff}} = 479.171$ (435.69) Gpa and $G_{\text{eff}} = 228.65$ Gpa (200.91). For the Gr(h-BN)/Liza-2D slab/Gr(h-BN) composite, the estimations of Y_{eff} and G_{eff} are 630.09 GPa (568.15 GPa) and 285.42 GPa (245.70 GPa), respectively, where, in this case, the ratio f was obtained making $t_{Gr} \to 2t_{Gr}$ in Equation (9).

In Figure 3 we compare our results obtained from DFT with those obtained from ROM. In this case, we focus on only two composites, (i) Lizardite reinforced by a single layer of Gr/BN and (ii) Lizardite reinforced by a double layer of Gr/BN. The two single-layer composites yielded comparable results. In (a) we represent the Young's and shear moduli for Liza-Gr2 and Liza-Gr3, which were calculated using DFT and Equations (7)–(9), where the Young's modulus Y(DFT) and shear modulus G(DFT) obtained from DFT are presented in blue and gray, respectively. The values Y(ROM) and G(ROM), calculated by ROM, are presented in brown and yellow, respectively. The corresponding results for the same superstructure reinforced with h-BN instead of Gr are shown in (b). We observe that the estimation results from Equations (7)–(9) are in reasonable agreement with the DFT results. If the Gr (h-BN) sheet is well separated from the lizardite slab, the results of Equations (7)–(9) would be exact. However, although weak, interactions exist between the Gr (h-BN) sheet and the lizardite slab, producing internal stress. The above equations work better for materials without misfit and with the same Poisson ratio [84]; therefore, the stresses that arise due to the difference between the Poisson ratio of GR (0.18) or h-BN (0.26) and the lizardite slab (0.36) contribute to reducing the accuracy of the above estimations.

This study demonstrates that stacking 2D materials like graphene (Gr) and hexagonal boron nitride (h-BN) onto a lizardite slab significantly enhances their mechanical properties, opening the door to creating new, stronger, and more versatile composite materials. The improved bulk, Young's, and shear moduli of these composites suggest they could be used in various high-performance applications, such as in the construction industry, due to their lightweight and superior mechanical strength.

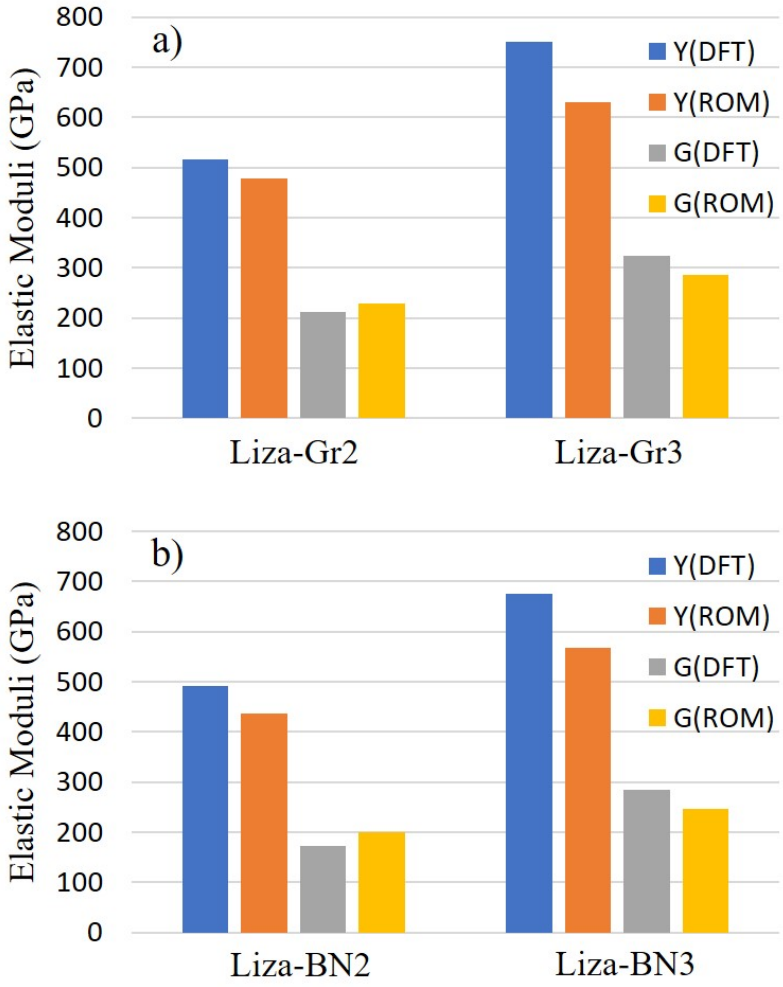

Figure 3. Comparison of the Young's and shear moduli of the composites obtained by the DFT method and estimated by the Rule of Mixtures (ROM): (**a**) lizardite slab reinforced by Gr; (**b**) lizardite slab reinforced by h-BN. In both figures, Y(DFT) and G(DFT) (Y(ROM) and G(ROM)) represent the Young's and shear moduli obtained by DFT (estimated by ROM).

4. Conclusions

We investigated the mechanical properties of a lizardite slab reinforced by graphene (Gr) or hexagonal boron nitride (h-BN) sheets using ab initio calculations based on density functional theory (DFT), obtaining the following results:

- Reinforcement with Gr or h-BN enhances the bulk, Young's, and shear moduli of the Liza-Gr1, Liza-Gr2, Liza-Gr3, Liza-BN1, Liza-BN2, and Liza-BN3 superstructures compared to the pristine lizardite slab.
- Given the weak van der Waals interactions between the Gr or h-BN monolayers and the lizardite slab surface, we estimated the Young's and shear moduli of the composites using the Rule of Mixtures. These estimations showed reasonable agreement with the DFT calculations.
- The enhanced mechanical properties demonstrate the designability of reinforced lizardite slabs, providing a platform for creating strong and tough 2D materials.
- These findings are vital for advancing various industries by ensuring safety, efficiency, and innovation in technological applications.

Author Contributions: A.K.C.M.: Conceptualization. C.A.d.F.: Conceptualization and Resources. C.M.: Resources. A.G.: Review and editing. H.O.d.F.: Investigation, conceptualization and writing. All authors have read and agreed to the published version of the manuscript.

Funding: This research received no external funding

Data Availability Statement: The data supporting the findings of this study are available upon request from the authors.

Acknowledgments: We acknowledge the financial support from the Brazilian funding agencies CAPES—Finance code 001, FAPEAM and CNPq.

Conflicts of Interest: The authors declare no conflicts of interest.

References

1. Novoselov, K.S.; Geim, A.K.; Morozov, S.V.; Jiang, D.E.; Zhang, Y.; Dubonos, S.V.; Grigorieva, I.V.; Firsov, A.A. Electric field effect in atomically thin carbon films. *Science* **2004**, *306*, 666–669. [CrossRef]
2. Novoselov, K.S.; Jiang, D.; Schedin, F.; Booth, T.; Khotkevich, V.; Morozov, S.; Geim, A.K. Two-dimensional atomic crystals. *Proc. Natl. Acad. Sci. USA* **2005**, *102*, 10451–10453. [CrossRef]
3. Neto, A.C.; Guinea, F.; Peres, N.M.; Novoselov, K.S.; Geim, A.K. The electronic properties of graphene. *Rev. Mod. Phys.* **2009**, *81*, 109. [CrossRef]
4. Mounet, N.; Gibertini, M.; Schwaller, P.; Campi, D.; Merkys, A.; Marrazzo, A.; Sohier, T.; Castelli, I.E.; Cepellotti, A.; Pizzi, G.; et al. Two-dimensional materials from high-throughput computational exfoliation of experimentally known compounds. *Nat. Nanotechnol.* **2018**, *13*, 246–252. [CrossRef] [PubMed]
5. Xu, R.; Zou, X.; Liu, B.; Cheng, H.M. Computational design and property predictions for two-dimensional nanostructures. *Mater. Today* **2018**, *21*, 391–418. [CrossRef]
6. Ma, Y.; Li, B.; Yang, S. Ultrathin two-dimensional metallic nanomaterials. *Mater. Chem. Front.* **2018**, *2*, 456–467. [CrossRef]
7. Dong, R.; Kuljanishvili, I. Progress in fabrication of transition metal dichalcogenides heterostructure systems. *J. Vac. Sci. Technol. B* **2017**, *35*, 030803. [CrossRef] [PubMed]
8. Choi, W.; Choudhary, N.; Han, G.H.; Park, J.; Akinwande, D.; Lee, Y.H. Recent development of two-dimensional transition metal dichalcogenides and their applications. *Mater. Today* **2017**, *20*, 116–130. [CrossRef]
9. Manzeli, S.; Ovchinnikov, D.; Pasquier, D.; Yazyev, O.V.; Kis, A. 2D transition metal dichalcogenides. *Nat. Rev. Mater.* **2017**, *2*, 17033. [CrossRef]
10. Saito, Y.; Nojima, T.; Iwasa, Y. Highly crystalline 2D superconductors. *Nat. Rev. Mater.* **2016**, *2*, 16094. [CrossRef]
11. Dean, C.; Young, A.; Wang, L.; Meric, I.; Lee, G.H.; Watanabe, K.; Taniguchi, T.; Shepard, K.; Kim, P.; Hone, J. Graphene based heterostructures. *Solid State Commun.* **2012**, *152*, 1275–1282. [CrossRef]
12. Wang, H.; Liu, F.; Fu, W.; Fang, Z.; Zhou, W.; Liu, Z. Two-dimensional heterostructures: Fabrication, characterization, and application. *Nanoscale* **2014**, *6*, 12250–12272. [CrossRef]
13. Androulidakis, C.; Zhang, K.; Robertson, M.; Tawfick, S. Tailoring the mechanical properties of 2D materials and heterostructures. *2D Mater.* **2018**, *5*, 032005. [CrossRef]
14. Hu, Z.; Liu, Z.B.; Tian, J.G. Stacking of exfoliated two-dimensional materials: A review. *Chin. J. Chem.* **2020**, *38*, 981–995. [CrossRef]
15. Liu, Y.; Weiss, N.O.; Duan, X.; Cheng, H.C.; Huang, Y.; Duan, X. Van der Waals heterostructures and devices. *Nat. Rev. Mater.* **2016**, *1*, 16042. [CrossRef]
16. Liao, W.; Huang, Y.; Wang, H.; Zhang, H. Van der Waals heterostructures for optoelectronics: Progress and prospects. *Appl. Mater. Today* **2019**, *16*, 435–455. [CrossRef]
17. Geim, A.K.; Grigorieva, I.V. Van der Waals heterostructures. *Nature* **2013**, *499*, 419–425. [CrossRef] [PubMed]
18. Frank, I.; Tanenbaum, D.M.; van der Zande, A.M.; McEuen, P.L. Mechanical properties of suspended graphene sheets. *J. Vac. Sci. Technol. B Microelectron. Nanometer Struct. Process. Meas. Phenom.* **2007**, *25*, 2558–2561. [CrossRef]
19. Poot, M.; van der Zant, H.S. Nanomechanical properties of few-layer graphene membranes. *Appl. Phys. Lett.* **2008**, *92*, 063111. [CrossRef]
20. Lee, C.; Wei, X.; Kysar, J.W.; Hone, J. Measurement of the elastic properties and intrinsic strength of monolayer graphene. *Science* **2008**, *321*, 385–388. [CrossRef]
21. Falin, A.; Cai, Q.; Santos, E.J.; Scullion, D.; Qian, D.; Zhang, R.; Yang, Z.; Huang, S.; Watanabe, K.; Taniguchi, T.; et al. Mechanical properties of atomically thin boron nitride and the role of interlayer interactions. *Nat. Commun.* **2017**, *8*, 15815. [CrossRef]
22. Bertolazzi, S.; Brivio, J.; Kis, A. Stretching and breaking of ultrathin MoS_2. *ACS Nano* **2011**, *5*, 9703–9709. [CrossRef] [PubMed]

23. Yang, Y.; Li, X.; Wen, M.; Hacopian, E.; Chen, W.; Gong, Y.; Zhang, J.; Li, B.; Zhou, W.; Ajayan, P.M.; et al. Brittle Fracture of 2D $MoSe_2$. *Adv. Mater. (Deerfield Beach Fla.)* **2016**, *29*, 1604201. [CrossRef]
24. Liu, K.; Yan, Q.; Chen, M.; Fan, W.; Sun, Y.; Suh, J.; Fu, D.; Lee, S.; Zhou, J.; Tongay, S.; et al. Elastic properties of chemical-vapor-deposited monolayer MoS_2, WS_2, and their bilayer heterostructures. *Nano Lett.* **2014**, *14*, 5097–5103. [CrossRef]
25. Li, Y.; Yu, C.; Gan, Y.; Jiang, P.; Yu, J.; Ou, Y.; Zou, D.F.; Huang, C.; Wang, J.; Jia, T.; et al. Mapping the elastic properties of two-dimensional MoS_2 via bimodal atomic force microscopy and finite element simulation. *NPJ Comput. Mater.* **2018**, *4*, 49. [CrossRef]
26. Chen, W.; Yang, T.; Dong, L.; Elmasry, A.; Song, J.; Deng, N.; Elmarakbi, A.; Liu, T.; Lv, H.B.; Fu, Y.Q. Advances in graphene reinforced metal matrix nanocomposites: Mechanisms, processing, modelling, properties and applications. *Nanotechnol. Precis. Eng.* **2020**, *3*, 189–210. [CrossRef]
27. Zhang, Z.; Li, T. Determining graphene adhesion via substrate-regulated morphology of graphene. *J. Appl. Phys.* **2011**, *110*, 083526. [CrossRef]
28. Yang, Y.; Rigdon, W.; Huang, X.; Li, X. Enhancing graphene reinforcing potential in composites by hydrogen passivation induced dispersion. *Sci. Rep.* **2013**, *3*, 2086. [CrossRef] [PubMed]
29. Ju, J.M.; Wang, G.; Sim, K.H. Facile synthesis of graphene reinforced Al matrix composites with improved dispersion of graphene and enhanced mechanical properties. *J. Alloys Compd.* **2017**, *704*, 585–592. [CrossRef]
30. Liu, J.; Zhang, Y.; Zhang, H.; Yang, J. Mechanical properties of graphene-reinforced aluminium composite with modified substrate surface: A molecular dynamics study. *Nanotechnology* **2020**, *32*, 085712. [CrossRef] [PubMed]
31. Wang, X.; Xiao, W.; Wang, L.; Shi, J.; Sun, L.; Cui, J.; Wang, J. Investigation on mechanical behavior of multilayer graphene reinforced aluminum composites. *Phys. E Low-Dimens. Syst. Nanostruct.* **2020**, *123*, 114172. [CrossRef]
32. Bhattacharya, M. Polymer nanocomposites—A comparison between carbon nanotubes, graphene, and clay as nanofillers. *Materials* **2016**, *9*, 262. [CrossRef] [PubMed]
33. Papageorgiou, D.G.; Li, Z.; Liu, M.; Kinloch, I.A.; Young, R.J. Mechanisms of mechanical reinforcement by graphene and carbon nanotubes in polymer nanocomposites. *Nanoscale* **2020**, *12*, 2228–2267. [CrossRef]
34. Güler, Ö.; Bağcı, N. A short review on mechanical properties of graphene reinforced metal matrix composites. *J. Mater. Res. Technol.* **2020**, *9*, 6808–6833. [CrossRef]
35. Wang, F.; Drzal, L.T.; Qin, Y.; Huang, Z. Enhancement of fracture toughness, mechanical and thermal properties of rubber/epoxy composites by incorporation of graphene nanoplatelets. *Compos. Part A Appl. Sci. Manuf.* **2016**, *87*, 10–22. [CrossRef]
36. Shao, L.; Li, J.; Guang, Y.; Zhang, Y.; Zhang, H.; Che, X.; Wang, Y. PVA/polyethyleneimine-functionalized graphene composites with optimized properties. *Mater. Des.* **2016**, *99*, 235–242. [CrossRef]
37. Cheng, Y.; Zhang, Y.; Wan, T.; Yin, Z.; Wang, J. Mechanical properties and toughening mechanisms of graphene platelets reinforced Al2O3/TiC composite ceramic tool materials by microwave sintering. *Mater. Sci. Eng. A* **2017**, *680*, 190–196. [CrossRef]
38. Wu, W.; Gui, J.; Sai, W.; Xie, Z. The reinforcing effect of graphene nano-platelets on the cryogenic mechanical properties of GNPs/Al2O3 composites. *J. Alloys Compd.* **2017**, *691*, 778–785. [CrossRef]
39. Zhi, C.; Bando, Y.; Tang, C.; Kuwahara, H.; Golberg, D. Large-scale fabrication of boron nitride nanosheets and their utilization in polymeric composites with improved thermal and mechanical properties. *Adv. Mater.* **2009**, *21*, 2889–2893. [CrossRef]
40. Khan, U.; May, P.; O'Neill, A.; Bell, A.P.; Boussac, E.; Martin, A.; Semple, J.; Coleman, J.N. Polymer reinforcement using liquid-exfoliated boron nitride nanosheets. *Nanoscale* **2013**, *5*, 581–587. [CrossRef]
41. Wang, X.; Zhi, C.; Li, L.; Zeng, H.; Li, C.; Mitome, M.; Golberg, D.; Bando, Y. "Chemical Blowing" of Thin-Walled Bubbles: High-Throughput Fabrication of Large-Area, Few-Layered BN and C x-BN Nanosheets. *Adv. Mater.* **2011**, *35*, 4072–4076. [CrossRef] [PubMed]
42. Lee, D.; Lee, B.; Park, K.H.; Ryu, H.J.; Jeon, S.; Hong, S.H. Scalable exfoliation process for highly soluble boron nitride nanoplatelets by hydroxide-assisted ball milling. *Nano Lett.* **2015**, *15*, 1238–1244. [CrossRef]
43. Jan, R.; May, P.; Bell, A.P.; Habib, A.; Khan, U.; Coleman, J.N. Enhancing the mechanical properties of BN nanosheet–polymer composites by uniaxial drawing. *Nanoscale* **2014**, *6*, 4889–4895. [CrossRef]
44. Wang, J.; Li, Z.; Fan, G.; Pan, H.; Chen, Z.; Zhang, D. Reinforcement with graphene nanosheets in aluminum matrix composites. *Scr. Mater.* **2012**, *66*, 594–597. [CrossRef]
45. Rashad, M.; Pan, F.; Tang, A.; Asif, M. Effect of graphene nanoplatelets addition on mechanical properties of pure aluminum using a semi-powder method. *Prog. Nat. Sci. Mater. Int.* **2014**, *24*, 101–108. [CrossRef]
46. Mellini, M. The crystal structure of lizardite 1 T: Hydrogen bonds and polytypism. *Am. Mineral.* **1982**, *67*, 587–598.
47. Schoonheydt, R.A.; Umemura, Y. Clay minerals as natural nanosheets. In *Inorganic Nanosheets and Nanosheet-Based Materials: Fundamentals and Applications of Two-Dimensional Systems*; Springer: Tokyo, Japan, 2017; pp. 33–53. [CrossRef]
48. Li, W.; Li, W.; Li, B.; Bai, Z. Electrolysis and heat pretreatment methods to promote CO_2 sequestration by mineral carbonation. *Chem. Eng. Res. Des.* **2009**, *87*, 210–215. [CrossRef]

49. McKelvy, M.J.; Chizmeshya, A.V.; Diefenbacher, J.; Béarat, H.; Wolf, G. Exploration of the role of heat activation in enhancing serpentine carbon sequestration reactions. *Environ. Sci. Technol.* **2004**, *38*, 6897–6903. [CrossRef] [PubMed]
50. Kharchafi, A.; Dahmani, J.; Tanji, K.; El Gaidoumi, A.; Iboustaten, E.; Fahoul, Y.; Belghiti, M.; El Mrabet, I.; Arrahli, A.; Kherbeche, A. Lizardite's capacity for carbon dioxide sequestration through a mineral process. *React. Kinet. Mech. Catal.* **2024**, *137*, 339–358. [CrossRef]
51. Carmignano, O.R.D.R.; Vieira, S.S.; Brandão, P.R.G.; Bertoli, A.C.; Lago, R.M. Serpentinites: Mineral structure, properties and technological applications. *J. Braz. Chem. Soc.* **2020**, *31*, 2–14. [CrossRef]
52. Giannozzi, P.; Baroni, S.; Bonini, N.; Calandra, M.; Car, R.; Cavazzoni, C.; Ceresoli, D.; Chiarotti, G.L.; Cococcioni, M.; Dabo, I.; et al. QUANTUM ESPRESSO: A modular and open-source software project for quantum simulations of materials. *J. Phys. Condens. Matter* **2009**, *21*, 395502. [CrossRef]
53. Payne, M.C.; Teter, M.P.; Allan, D.C.; Arias, T.; Joannopoulos, A.J. Iterative minimization techniques for ab initio total-energy calculations: Molecular dynamics and conjugate gradients. *Rev. Mod. Phys.* **1992**, *64*, 1045. [CrossRef]
54. Grimme, S. Accurate description of van der Waals complexes by density functional theory including empirical corrections. *J. Comput. Chem.* **2004**, *25*, 1463–1473. [CrossRef]
55. Grimme, S. Semiempirical GGA-type density functional constructed with a long-range dispersion correction. *J. Comput. Chem.* **2006**, *27*, 1787–1799. [CrossRef] [PubMed]
56. Monkhorst, H.J.; Pack, J.D. Special points for Brillouin-zone integrations. *Phys. Rev. B* **1976**, *13*, 5188. [CrossRef]
57. Pack, J.D.; Monkhorst, H.J. "Special points for Brillouin-zone integrations"—A reply. *Phys. Rev. B* **1977**, *16*, 1748. [CrossRef]
58. Momma, K.; Izumi, F. VESTA 3 for three-dimensional visualization of crystal, volumetric and morphology data. *J. Appl. Crystallogr.* **2011**, *44*, 1272–1276. [CrossRef]
59. Voigt, W. *Lehrbuch der Kristallphysik (mit Ausschluss der Kristalloptik)*; B.G. Teubner: Leipzig/Berlin, Germany, 2010.
60. Dal Corso, A. Available online: https://dalcorso.github.io/thermo_pw/ (accessed on 25 November 2024).
61. Bower, A.F. *Applied Mechanics of Solids*; CRC Press: Boca Raton, FL, USA, 2010.
62. Born, M. On the stability of crystal lattices. I. In *Mathematical Proceedings of the Cambridge Philosophical Society*; Cambridge University Press: Cambridge, UK, 1940; Volume 36, pp. 160–172.
63. Mouhat, F.; Coudert, F.X. Necessary and sufficient elastic stability conditions in various crystal systems. *Phys. Rev. B* **2014**, *90*, 224104. [CrossRef]
64. Nye, J.F. *Physical Properties of Crystals: Their Representation by Tensors and Matrices*; Oxford University Press: Oxford, UK, 1985.
65. Liu, K.; Wu, J. Mechanical properties of two-dimensional materials and heterostructures. *J. Mater. Res.* **2016**, *31*, 832–844. [CrossRef]
66. Hill, R. The elastic behaviour of a crystalline aggregate. *Proc. Phys. Soc. Sect. A* **1952**, *65*, 349. [CrossRef]
67. Andrew, R.C.; Mapasha, R.E.; Ukpong, A.M.; Chetty, N. Mechanical properties of graphene and boronitrene. *Phys. Rev. B* **2012**, *85*, 125428. [CrossRef]
68. Chaikin, P.M.; Lubensky, T.C.; Witten, T.A. *Principles of Condensed Matter Physics*; Cambridge University Press: Cambridge, UK, 1995; Volume 10.
69. Malgrange, C.; Ricolleau, C.; Schlenker, M. *Symmetry and Physical Properties of Crystals*; Springer: Dordrecht, The Netherlands; Berlin/Heidelberg, Germany; New York, NY, USA; London, UK, 2014; p. 296. [CrossRef]
70. Singh, S.; Espejo, C.; Romero, A.H. Structural, electronic, vibrational, and elastic properties of graphene/MoS_2 bilayer heterostructures. *Phys. Rev. B* **2018**, *98*, 155309. [CrossRef]
71. Auwärter, W. Hexagonal boron nitride monolayers on metal supports: Versatile templates for atoms, molecules and nanostructures. *Surf. Sci. Rep.* **2019**, *74*, 1–95.
72. Gusmão, M.S.; Gopal, P.; Siloi, I.; Curtarolo, S.; Fornari, M.; Nardelli, M.B. Mechanical properties of chemically modified clay. *Sci. Rep.* **2019**, *9*, 13698. [CrossRef]
73. Deng, X.; Luo, C.; Wentzcovitch, R.M.; Abers, G.A.; Wu, Z. Elastic anisotropy of lizardite at subduction zone conditions. *Geophys. Res. Lett.* **2022**, *49*, e2022GL099712. [CrossRef]
74. Reynard, B.; Hilairet, N.; Balan, E.; Lazzeri, M. Elasticity of serpentines and extensive serpentinization in subduction zones. *Geophys. Res. Lett.* **2007**, *34*, L13307. [CrossRef]
75. Hilairet, N.; Daniel, I.; Reynard, B. P–V equations of state and the relative stabilities of serpentine varieties. *Phys. Chem. Miner.* **2006**, *33*, 629–637. [CrossRef]
76. Duerloo, K.A.N.; Ong, M.T.; Reed, E.J. Intrinsic piezoelectricity in two-dimensional materials. *J. Phys. Chem. Lett.* **2012**, *3*, 2871–2876. [CrossRef]
77. Han, T.; Luo, Y.; Wang, C. Effects of temperature and strain rate on the mechanical properties of hexagonal boron nitride nanosheets. *J. Phys. D Appl. Phys.* **2013**, *47*, 025303. [CrossRef]
78. Cong, X.; Li, Q.Q.; Zhang, X.; Lin, M.L.; Wu, J.B.; Liu, X.L.; Venezuela, P.; Tan, P.H. Probing the acoustic phonon dispersion and sound velocity of graphene by Raman spectroscopy. *Carbon* **2019**, *149*, 19–24. [CrossRef]

79. Yang, W.; Zhao, Q.; Xin, L.; Qiao, J.; Zou, J.; Shao, P.; Yu, Z.; Zhang, Q.; Wu, G. Microstructure and mechanical properties of graphene nanoplates reinforced pure Al matrix composites prepared by pressure infiltration method. *J. Alloys Compd.* **2018**, *732*, 748–758. [CrossRef]
80. Monteiro, A.; Frota, H.; Frota, C.; Gusmão, M.; Ghosh, A. Analysis of lizardite-graphene van der Waals heterostructures: A DFT study. *Diam. Relat. Mater.* **2024**, *141*, 110677. [CrossRef]
81. Frota, H.; Chaudhuri, P.; Ghosh, A.; Frota, C. Lizardite–h-BN heterostructures—Application of clay minerals in technology. *J. Appl. Phys.* **2023**, *134*, 214301. [CrossRef]
82. Benedict, L.X.; Chopra, N.G.; Cohen, M.L.; Zettl, A.; Louie, S.G.; Crespi, V.H. Microscopic determination of the interlayer binding energy in graphite. *Chem. Phys. Lett.* **1998**, *286*, 490–496. [CrossRef]
83. Zacharia, R.; Ulbricht, H.; Hertel, T. Interlayer cohesive energy of graphite from thermal desorption of polyaromatic hydrocarbons. *Phys. Rev. B* **2004**, *69*, 155406. [CrossRef]
84. Clyne, T.W.; Withers, P.J. *An Introduction to Metal Matrix Composites*; Cambridge University Press: Cambridge, UK, 1993; p. 12.